

Full length article

Determination of the five parameter grain boundary character distribution of nanocrystalline alpha-zirconium thin films using transmission electron microscopy

I. Ghamarian ^{a, b, *}, P. Samimi ^{a, b}, G.S. Rohrer ^{c, 1}, P.C. Collins ^{a, b, d}^a Department of Materials Science and Engineering, Iowa State University, Ames, IA, 50011, USA^b Center for Advanced Non-Ferrous Structural Alloys, An NSF I/UCRC Between Iowa State University and the Colorado School of Mines, USA^c Department of Materials Science and Engineering, Carnegie Mellon University, Pittsburgh, PA, 15213, USA^d Ames Laboratory, Iowa State University, Ames, IA, 50011, USA

ARTICLE INFO

Article history:

Received 19 December 2016

Received in revised form

20 February 2017

Accepted 17 March 2017

Keywords:

Grain boundary character distribution

Zirconium

ASTAR™/PED

Thin film

Nanocrystalline

ABSTRACT

Grain boundary engineering and other fundamental materials science problems (e.g., phase transformations and physical properties) require an improvement in the understanding of the type and population of grain boundaries in a given system – yet, databases are limited in number and sparse in detail, including for *hcp* crystals such as zirconium. One way to rapidly obtain databases to analyze is to use small-grained materials and high spatial resolution orientation microscopy techniques, such as ASTAR™/precession electron diffraction. To demonstrate this, a study of grain boundary character distributions was conducted for α -zirconium deposited at room temperature on fused silica substrates using physical vapor deposition. The orientation maps of the nanocrystalline thin films were acquired by the ASTAR™/precession electron diffraction technique, a new transmission electron microscope based orientation microscopy method. The reconstructed grain boundaries were classified as pure tilt, pure twist, 180°-twist and 180°-tilt grain boundaries based on the distribution of grain boundary planes with respect to the angle/axis of misorientation associated with grain boundaries. The results of the current study were compared to the results of a similar study on α -titanium and the molecular dynamics results of grain boundary energy for α -titanium.

© 2017 Acta Materialia Inc. Published by Elsevier Ltd. All rights reserved.

1. Introduction

Grain boundary engineering (GBE) is used to improve certain material properties by controlling the population of grain boundary types [1–5]. For instance, the intergranular stress corrosion cracking in nickel-based alloys can be reduced by increasing the fraction of low Σ coincidence site lattice (Σ CSL) boundaries where Σ is the reciprocal of the number fraction of coincident sites [6]. For GBE to be successful, a comprehensive knowledge of the grain boundary structure and the population is required [7] as is their

influence on the properties of interest. However, developing the requisite knowledge of the grain boundaries, especially when considering large populations, has some intrinsic challenges [8–10]. For example, the three misorientation parameters used to determine the CSL boundary types are not sufficient to specify the coincidence degree in the grain boundary plane [11]. In addition, it has been shown that to interpret some phenomena (e.g., stored elastic strain [11]; pronounced differences in energies of coherent twin (i.e., $\Sigma 3$ boundary with a {111} boundary plane) as well as incoherent twin (i.e., $\Sigma 3$ boundary on a {112} boundary plane) [12]; and, intergranular stress corrosion [13]) both the misorientation and grain boundary plane distribution should be considered. Therefore, it is necessary to characterize both the grain boundary plane and the grain boundary misorientation to adequately characterize the boundaries so that precise interpretations can be made, and GBE can be affected [13].

The study of grain boundaries ranges from calculations of the atomic bonding and assessment of the chemical composition of the

* Corresponding author. Department of Materials Science and Engineering, Iowa State University, Ames, IA, 50011, USA.

E-mail addresses: imanghamarian@yahoo.com (I. Ghamarian), psamimi@iastate.edu (P. Samimi), rohrer@cmu.edu (G.S. Rohrer), pcollins@iastate.edu (P.C. Collins).

¹ Professor Gregory S. Rohrer was an editor of the journal during the review period of the article. To avoid a conflict of interest, Professor Irene J. Beyerlein acted as editor for this manuscript.

grain boundaries [14] to geometrical attributes including microscopic boundary parameters (e.g., translations between lattices form a grain boundary) [15] and macroscopic boundary parameters (e.g., misorientation between adjacent grains) [16]. The distribution of macroscopic grain boundary parameters may be determined from the orientation of the locations where grain boundaries intersect the plane of observation using a stereological method [17]. Each grain boundary is identified by five characteristic parameters. Three of these parameters specify the lattice misorientation Δg between the two crystals across a grain boundary. The misorientation space is parameterized into cells (or bins) with a specific discretization (e.g., 10°) using Bunge Euler angles ($\varphi_1, \Phi, \varphi_2$). The misorientation domain is parameterized by $\varphi_1, \cos(\Phi)$ and φ_2 within the range of 0 to $\pi/2$, 0 to 1 and 0 to $\pi/2$, respectively [18]. The other two parameters determine the inclination of the grain boundary normal n . The inclination of the boundary normal in the crystal reference frame is parameterized using two angles (i.e., θ and φ) in the spherical coordinate system. The two angles are parameterized by $\cos(\theta)$ and φ within the range of 0–1 and 0 to 2π , respectively. When parameterizing grain boundary space, the cell size should be large enough to contain a considerable number of observations per cell (or per bin) and small enough to represent the textural features at a sufficient resolution [18]. The grain boundary character distribution (GBCD) method is based on partitioning the boundary parameter space into bins of equal volume. Recently, a new GBCD method has been proposed which determines the grain boundary distribution based on counting boundaries which are closer than an angular distance threshold value to a specific point in the boundary space [19]. The grain boundary character distribution is defined as the distribution (λ) of boundaries with the misorientation of Δg and the boundary normal of n (i.e., $\lambda(\Delta g, n)$). GBCD is measured in the unit of multiples of a random distribution (MRD). Distribution values larger than one indicate frequencies of occurrence more than expected in a random distribution.

Based on GBCD studies in a wide range of materials (e.g., Al [20], MgAl_2O_4 [21], MgO [18], SrTiO_3 [22], TiO_2 [23], Fe-1%Si [24]), it was noticed that the distribution of grain boundary planes is anisotropic, where low-energy and low-index habit planes are more favorable and grain boundary energy (i.e., $\gamma(\Delta g, n)$) is inversely correlated to the grain boundary character distribution (i.e., $\lambda(\Delta g, n)$) [25–27] for randomly textured materials. GBCD studies of materials with *hcp* crystal structure are very limited. The limited research on the *hcp* systems includes the work of Kelly et al. [28] who showed that prismatic grain boundary planes are more prevalent than basal grain boundary planes for α -titanium. In this work, the population of 180° -twist and 180° -tilt grain boundaries was shown to be greater than what is expected for the random distribution for this material. Another GBCD study of α -titanium by Randle et al. [29] attributed the plane population peak associated with the 60° – 65° / $(2\bar{1}\bar{1}0)$ misorientation to the *bcc* to *hcp* (β to α) phase transformation in titanium. Beladi et al. [30] showed that the distribution of intervariant crystallographic planes in martensite for a Ti-6Al-4V alloy showed strong texture for prismatic planes, {hkil0}. They also showed the highest intervariant boundary populations were associated with 63.26° / $[\bar{1}055\bar{3}]$ and 60° / $[\bar{1}1\bar{2}0]$ which terminate on $(4, \bar{1}, \bar{3}, 0)$ ² and $(\bar{1}, 0, 1, 1)$. Notably, most of the GBCD studies have been conducted on cubic materials with the average grain size above the micron scale and very few GBCD investigations have been performed on nanocrystalline materials, although where studies have been made, the GBCD of the

nanoscaled material and microscaled material have been in agreement.³ For instance, GBCD results of nanocrystalline copper films [31] showed that a strong (111) peak for 60° / $[\bar{1}11]$ which is in accordance with a similar study on copper [32] with the average grain size far larger than the nanocrystalline copper films. Similarities between the GBCD results of metallic materials with nano and micron grain sizes were observed for nanocrystalline tungsten as well [33].

In general, electron backscattered diffraction (EBSD), a scanning electron microscope based orientation microscopy method, cannot be used for the characterization of grain boundaries in microstructures where the average grain size of less than a critical dimension, as there is a minimum number of indexed points required for subsequent analyses. For example, this critical dimension has been reported to be ~ 100 nm for iron, and is attributed to the spatial resolution in the *x* direction (35 ± 5 nm) and in the *y* direction (90 ± 15 nm, i.e., the lateral resolution) [31,34]. The precise spatial resolution in EBSD is primarily a function of the atomic number and the accelerating voltage, but can be calculated easily using Monte Carlo approaches of electron beam/specimen interactions. Also, it is important to note that there is an apparent inconsistency between the spatial resolution and the grain size that may be studied. In reality, this minimum grain size is likely to approach ~ 500 nm, once the number of measurements/grain is sufficiently large for statistically reliable analyses. This relatively poor spatial resolution results in an inability to detect fine features (e.g., nanotwins) [35,36]. Recently, transmission EBSD (t-EBSD) [37] or transmission Kikuchi diffraction (TKD) [38] technique has been developed which enjoys the spatial resolution of ~ 2 nm. However, due to the unusual projection geometry, the angular resolution of this SEM based orientation microscopy technique is reported to be reduced to $\sim 1^\circ$ [39].

ASTAR™/precession electron diffraction (ASTAR™/PED) is a relatively new orientation microscopy technique that is implemented onto transmission electron microscopes and makes possible the characterization of very fine features due to the spatial resolution of ~ 2 nm [40] and the angular resolution of $\sim 0.3^\circ$ [41] or $\sim 0.8^\circ$ [40]. This technique has been used successfully to characterize materials which cannot be studied by EBSD (e.g., severely deformed metallic materials [42] or grain growth characterization at the nanoscale regime [43]). By precessing the direct beam, the accuracy of indexing improves considerably as any dynamical diffraction effects are reduced or eliminated, and a quasi-kinematical diffraction condition [41,44] operates, which makes the acquired diffraction patterns sharper and reduces/removes Kikuchi lines, double diffraction events, and significantly reduces the background from the recorded diffraction patterns [45]. Also, by precessing the direct beam, the 180° ambiguity problem of indexing spot diffraction patterns is avoided, as higher order Laue zone reflections are excited in addition to zero order Laue zone reflections [46].

The orientation datasets used for GBCD studies have been prepared by different characterization techniques. For instance, EBSD technique was used to prepare 2D orientation datasets [12] while the combination of EBSD and serial sectioning technique using focused ion beam was used to prepare 3D orientation datasets for materials with the average grain size of few microns [47]. However, since the preparation of 3D datasets using the combination of focused ion beam and EBSD techniques is very time-consuming, recently Xe plasma focused ion beam was used to prepare 3D orientation datasets in a considerably shorter time [28]. For the

² It is common to deviate from low index poles when conducting GBCD studies. To ease in the readability of planes, the authors have adopted the style of including commas in the Miller indices designations for *hcp* four-index notation.

³ It is expected that small differences in solute levels of elements that partition to the grain boundaries may influence the GBCD of some systems.

case of nanocrystalline materials, ASTAR™/PED technique was used to prepare 2D orientation datasets for copper and tungsten [31,33].

In this paper, a quantitative study of the GBCD in thin zirconium films was conducted using ASTAR™/PED technique with subsequent statistical analyses.

2. Experimental approaches

Twelve 3 mm × 3 mm × 6.3 mm fused silica substrates were cleaned in an ultrasonic bath of acetone for 15 min and then rinsed with isopropanol after which they were dried individually with flowing dry nitrogen. The substrates were loaded into a PVD Products sputter deposition machine, sputter down configuration, and held vertically on a rotatable platen, exposing only the 3 mm × 3 mm portion of the fused silica. The machine was pumped down to 10⁻⁵ Pa before introducing 20 standard cubic centimeters per minute of argon gas controlled by a mass flow controller. A closed-loop pressure control system, which utilizes a stepper motor controlled gate valve in conjunction with a capacitance manometer, controlled the pressure in the system at 0.66 Pa. A shuttered PVD Products 5-cm magnetron loaded with a 6.3 mm thick zirconium target, held 127 mm away from the substrates, was then turned on with 150 W of DC power. After conditioning the target for 300 s, and with the substrates rotating to increase uniformity among them, the shutter was opened for 435 s, to deposit 130 nm of zirconium on the fused silica substrates at room temperature. The deposition length was determined by measuring the sputtering rate in a previous setup run using a profilometer to measure the step height, and thus thickness, of a masked silicon wafer.

Thin foils for orientation microscopy were prepared parallel to the coating surface using dual-beam focused ion beam (FIB), specifically an FEI Nova Nanolab 200 system. The orientation microscopy was conducted on an FEI Tecnai G2 F20 S-Twin FEG scanning/transmission electron microscope operating at 200 keV using ASTAR™/PED (Nanolab, Brussels, Belgium) hardware and data acquisition software packages. The direct electron beam was precessed for 0.3° at a TEM spot size of nine (which is equivalent to ~1 nm on the FEI Tecnai [48]). Orientation microscopy scans were conducted at the step size of 2 nm. An external high frame rate camera (Stingray F-046, Allied Vision Technologies) was used to record the spot diffraction patterns. Each spot diffraction pattern was recorded as a 144 × 144 pixel image at the exposure time of 60 ms and the camera length of 71 mm. Simulated diffraction patterns (templates) were made for the α -zirconium phase ($a = 0.323$ nm and $c = 0.514$ nm, $P6_3/mmc$) at the operating accelerating voltage of 200 keV. The acquired diffraction pattern images were indexed (i.e., assigning a Bunge Euler angle set to each recorded diffraction pattern image) by cross correlating more than 5000 templates with each image and finding the most matched template⁴ [41]. An orientation file was generated as a result of indexing recorded diffraction patterns and subsequently assigning Bunge Euler angle sets to the recorded diffraction patterns. The orientation files were exported to TexSEM laboratories Orientation Imaging (TSL OIM™, EDAX, Mahwah, USA) analysis software for further post processing.

Since the absolute orientation of grains is required in GBCD studies, it is essential to determine the sample reference frame with respect to the acquired orientation. The reference frame calibration was done by following three consecutive steps: (a) finding the rotation between an image and its diffraction pattern (rotation-

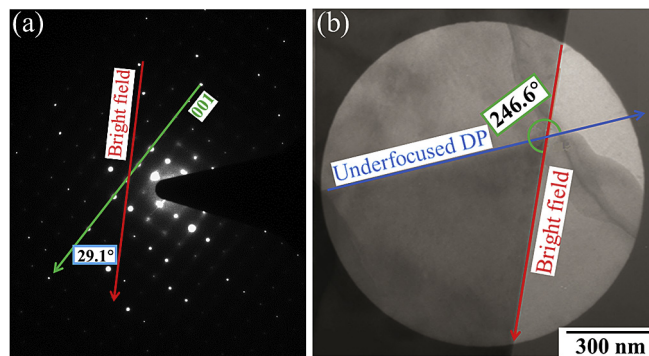


Fig. 1. (a) The red arrow represents the growth direction (i.e., [001]) of MoO₃ in the bright field image and the green arrow shows the same direction in the diffraction pattern image (b) directions of an arbitrary feature in the bright field image (red arrow) and the same feature in the underfocused diffraction pattern image are displayed. (For interpretation of the references to colour in this figure legend, the reader is referred to the web version of this article.)

calibration experiment [49]) (b) addressing the 180° ambiguity problem and (c) aligning the TSL OIM™ reference frame to ASTAR™ reference frame. Due to the importance of absolute orientation determination (and their general absence in the literature), these steps are explained clearly below.

The rotation-calibration experiment was conducted using a crystal of α -MoO₃ (orthorhombic crystal structure) which grows along [001] direction. Initially, a bright field image was captured using a Gatan CCD camera at a magnification of 13,500×, the same magnification as used for the data acquisition of the α -zirconium. A diffraction pattern at the camera length of 71 mm was acquired as well. The rotation angle between the diffraction pattern and the bright field image along the [001] direction was determined to be 29.1°, Fig. 1(a). Given the 180° ambiguity problem, it is never clear whether the necessary rotation is 29.1° or 209.1° (i.e., ω or $180^\circ + \omega$). To solve the 180° ambiguity problem, the rotation required to overlap an arbitrary feature in a bright field image and the same feature in the underfocused⁵ diffraction pattern image was determined, Fig. 1(b). Since the rotation angle measured here (246.6°) is larger than 180°, the 180° ambiguity is present, and thus a rotation of 209.1° (i.e., $180^\circ + 29.1^\circ$) must be applied as the first step (i.e., rotation-calibration). This rotation is applied to the first term of each Bunge Euler angle set (i.e., ϕ_1). The last step involves the reference frame calibration. In this step, the TSL OIM™ reference frame is aligned with the ASTAR™ reference frame. As shown in Fig. 2, while the scan frame of TSL OIM™ and ASTAR™ are the same, a 90° rotation along the normal direction (ND) is required to align the Euler frame of TSL OIM™ with respect to the Euler frame of ASTAR™. Therefore, the orientation datasets were rotated +90 counter-clockwise active rotation along the normal direction to coincide the ASTAR™ and TSL OIM™ reference frames [48].

Since occasionally the recorded diffraction patterns may be indexed incorrectly due to the low intensity of the diffraction spots (with respect to the background intensity of the acquired image) or few diffraction spots within a recorded image, the orientation datasets were cleaned up to correct the spurious points. To ensure that no artificial grain formed by incorrectly indexing of the diffraction patterns, a grain dilation clean up procedure with a minimum grain size of 10 pixels in multiple rows was used. Subsequently, the neighbor orientation correlation (level 4) clean up

⁴ The 0.3° or 0.8° angular resolution is the experimental limit of the resolution by ASTAR™/PED technique and it is independent of the number of templates used for indexing the diffraction pattern images.

⁵ clockwise and counterclockwise rotations of the focus knob in FEI and JOEL microscopes, respectively.

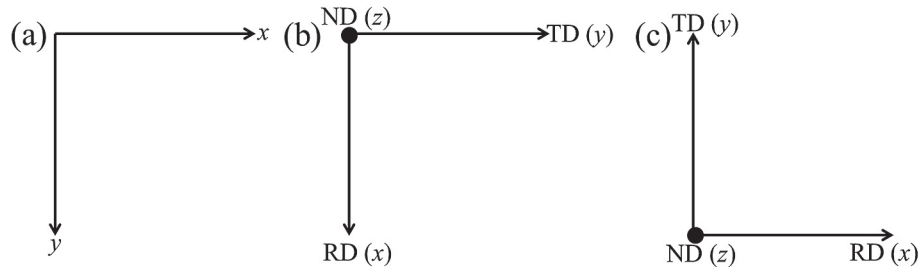


Fig. 2. (a) ASTAR™ and TSL OIM™ scan frames (b) TSL OIM™ Euler frame (c) ASTAR™ Euler frame are shown.

procedure in TSL OIM™ software was applied to the orientation dataset [31]. This clean up procedure determines the more likely orientations for points with the confidence index of less than 0.1 [50]. Notably, the average confidence index of the orientation datasets was ~ 0.4 . The orientation distribution map for one of the datasets is presented in Fig. 3(a), after the data has been processed by the previously described clean up algorithms. A total of seven datasets were collected from the same α -zirconium sample in order to provide sufficient counting statistics for the subsequent analysis. Our datasets, once merged, contain 57,019 unique grains. All the orientation datasets were merged to determine the overall texture for all the orientation datasets, Fig. 3(b). The maximum magnitude of the texture in the current study is similar to another GBCD study related to materials with *hcp* crystal structure [28].

An assumption was made regarding the grain shapes for the current study. It was assumed that these α -zirconium grains are columnar whose grain boundaries normal are perpendicular to the electron beam direction. This assumption was validated based on the width of the trace of grain boundary planes on the observation plane as follows. The thickness of the thin foils prepared for PED-based orientation microscopy analyses was ~ 100 nm. Based on the schematic presented in Fig. 4(a), the width of the traces associated with grain boundary planes inclined for 5° and 10° from the observation plane normal is 8.7 nm and 17.6 nm, respectively. The width of a grain boundary trace can be measured directly from an index map which is analogous to the image quality map of EBSD. A portion of an index map associated with one of the orientation datasets collected in this study is presented in Fig. 4(b). For a better

visualization, the area surrounded by the yellow rectangle was enlarged and presented in Fig. 4(c). It is clear that the grain boundary traces is less than 8.7 nm which indicates that the assumption of columnar grains is valid. For materials where this assumption fails, it will be necessary to assess the grain boundary plane on both the top and bottom of a specimen following, for example, an electron diffraction optical reflectance method [51].

To reconstruct grain boundary traces, the average orientation of each grain was assigned to all the points within the grain. Subsequently, 202,950 grain boundary traces were reconstructed with a tolerance of two pixels from all the collected orientation datasets following the method described by Wright and Larsen [52]. Owing to the step size (2 nm) and the possibility of incorporating spurious or otherwise uninterpretable grain boundaries, the boundary segments smaller than 4 nm in length were excluded from the datasets. The five-parameter GBCD space (i.e., ϕ_1 , Φ , ϕ_2 , θ and φ) was discretized with the resolution of 10° . This resolution of discretization results in 26,000 distinct boundaries. For an evenly distributed grain boundary dataset, seven to eight observations per grain boundary type is expected for a 202,950 reconstructed grain boundary dataset.

3. Results and discussion

While seminal work has been published for the grain boundaries of other *hcp* systems, specifically the molecular dynamics work of Wang and Beyerlein [53,54] on the atomic structures of magnesium and titanium grain boundaries, and the experimental

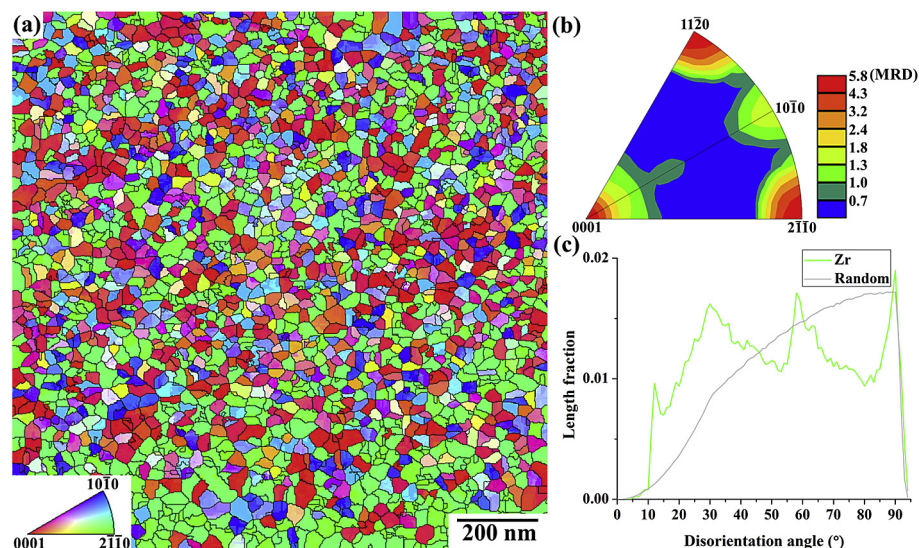


Fig. 3. (a) A plan-view ASTAR™/PED orientation distribution map of the zirconium thin film along the normal direction, (b) inverse pole figure for zirconium along the normal direction (MRD represents multiples of random distribution) and (c) distribution of disorientation angles for zirconium and random grain boundaries are shown.

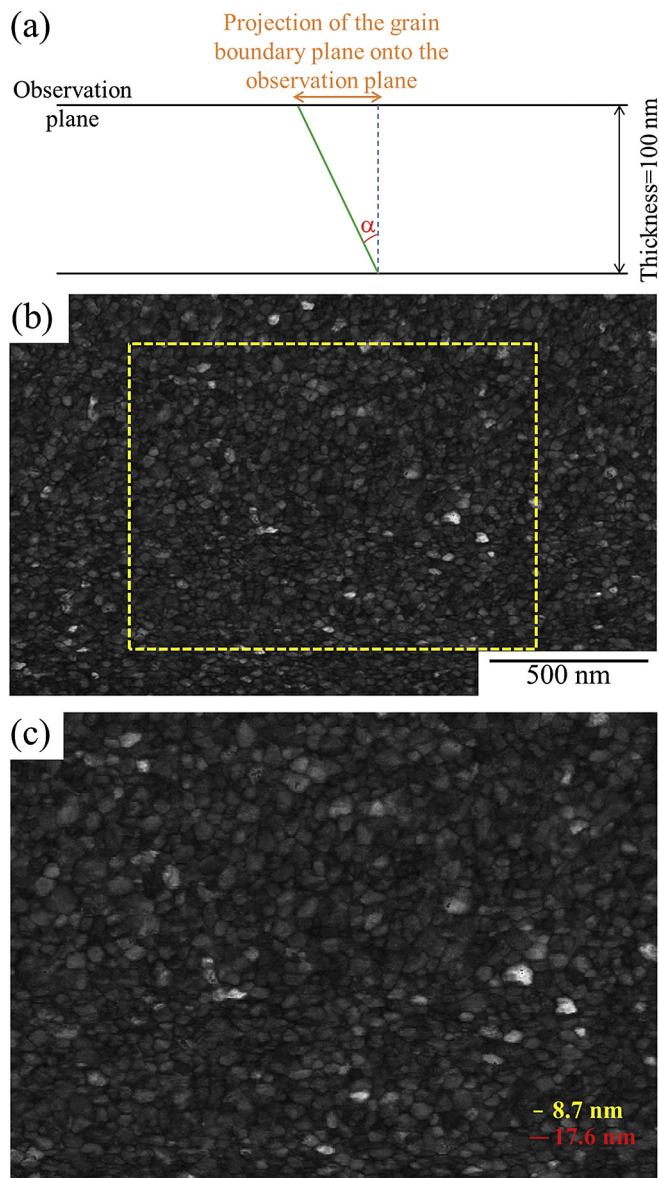


Fig. 4. (a) A schematic of an inclined grain boundary plane (b) a portion of an index map associated with one of the orientation microscopy scans and (c) the enlarged view of the area surrounded by the yellow square in part “b” are depicted. (For interpretation of the references to colour in this figure legend, the reader is referred to the web version of this article.)

work of Kelly et al. [28] on the GBCD of α -titanium, there has been little to no work in the published literature regarding zirconium. This dearth of knowledge presents a challenge in that little is known about specific low energy (and/or high population) boundary configurations for the α -zirconium system, yet in some cases, the literature can provide guidance when there are similarities with other systems. Indeed, given the similar c/a ratios of Ti and Zr (1.587 and 1.593, respectively) and their nominally ideal Poisson's ratio, it is reasonable to expect similarities in their GBCDs. Thus, in the absence of other information, comparisons are made with α -titanium. What follows represents work in which the data has been analyzed using two approaches. The first approach involves data-mining to determine high-population boundary configurations of zirconium that have not been observed. The second

approach draws upon the literature [28,53,54] to observe similarities, even though the material system is different.

The distributions of disorientation angles for the combined orientation dataset as well as a simulated random grain boundary dataset are presented in Fig. 3(c). In comparison to the random distribution, the current dataset has a larger population for disorientation angles which are less than 40° . This observation is consistent with the same analysis for the α -titanium [28]. Also, the length fraction of grain boundaries within the disorientation angle range of 57° – 60° is larger than it is for the random grain boundaries. Except for very large disorientation angles (i.e., $\sim 90^\circ$), the length fraction of the zirconium grain boundaries is less than the random populations for disorientation angles larger than 60° . This fact is accordant with a previous study on α -titanium [55].

The disorientation axes associated with fixed spans of the disorientation angles centered at a given value of $\pm 5^\circ$ are plotted in the equal area projection (Fig. 5). The population density of the disorientation axes within the disorientation angle range of 15° – 35° has major peaks corresponding to $\langle 0001 \rangle$ and $\langle 2\bar{1}\bar{1}0 \rangle$. Also, for the disorientation angle range of 25° – 35° , a disorientation axis peak close to $\langle 10\bar{1}0 \rangle$ is seen. Within the disorientation angle range of 35° – 95° , the population density of the disorientation axis along $\langle 2\bar{1}\bar{1}0 \rangle$ is more than the uniform (random) distribution. A peak close to $\langle 4\bar{1}31 \rangle$ is seen for the disorientation angle range of 85° – 95° . Notably, in the other crystallographic directions for the entire disorientation values, the distribution is almost uniform.

The grain boundary plane distribution of the experimentally measured data for α -zirconium in the crystal reference frame is plotted as a stereographic projection, Fig. 6. The relative peak intensity of the grain boundary plane distributions for the $\langle 0001 \rangle$, $\langle 10\bar{1}0 \rangle$ and $\langle 2\bar{1}\bar{1}0 \rangle$ planes are ~ 2 , ~ 1.8 and ~ 1.4 MRD, respectively. The difference between the maximum and minimum of the grain boundary plane distribution is ~ 1.5 MRD, revealing an anisotropic distribution of grain boundary planes. Notably, this difference for α -Ti [28], WC [56], MgO [18], Ni [57] and SrTiO₃ [22] has been reported to be 0.4 MRD, 3.7 MRD, 1.3 MRD, 2.1 MRD and 0.8 MRD, respectively.

The output of the GBCD analyses is incredibly data rich. For example, for every disorientation angle, it is possible to assess a large number of axes in the angle/axis sets (i.e., GBCD sections). Each GBCD section is effectively a stereographic projection consisting of color-represented information regarding the total population of grain boundary planes associated with an angle/axis set. The following sections (3.1–3.4) are detailed GBCD analyses and interpretations of specific disorientation angles which are over represented in Fig. 3(c) and the high population disorientation axes presented in Fig. 5.

3.1. GBCD sections about the $[0001]$ axis of misorientation

The GBCD section for the $13^\circ/[0001]$ misorientation is presented in Fig. 7(a). The stereographic representations for the calculated geometrically characteristic boundaries associated with the aforementioned angle/axis of misorientation are shown in Fig. 7(b). For the case of $13^\circ/[0001]$, the maximum peak corresponds to angles in close proximity of the center (i.e., the $\langle 0001 \rangle$ pole) with the intensity of 6 MRD. This diffusiveness of the poles (i.e., the appearance of streaks) as well as the absolute value of observation frequencies are affected by the binning (cell) size and the angular resolution of the characterization technique. Notably, the center of the GBCD plot shown in Fig. 7(a), which represents a pure twist grain boundary, does not have a high observation frequency.

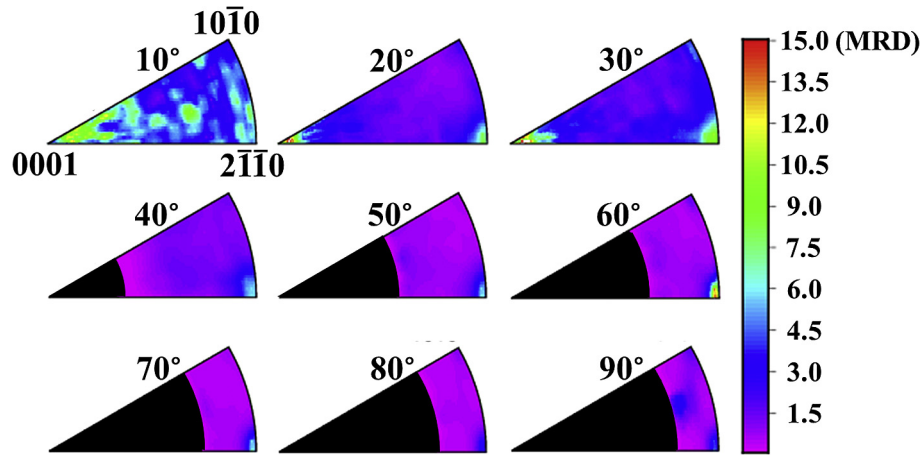


Fig. 5. The distribution of disorientation axis for zirconium within fixed intervals of the disorientation angle is presented.

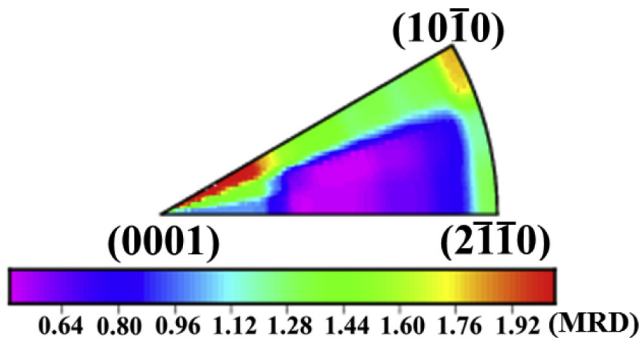


Fig. 6. The distribution of grain boundary planes is presented. Notably, all the stereographic projections presented in this study follow the convention shown in this plot.

Also, 180° -twist grain boundaries with a $(\bar{1},8,\bar{7},0)$ grain boundary plane orientation and its symmetrically equivalent positions have a population of ~ 4.2 MRD⁶ [58,59] as well as 180° -tilt grain boundaries are observed with a population of ~ 2.5 MRD.

In addition to the highly complex nature of grain boundary energy functions and measurable populations for different experiments, in this study since the sample (and thus the orientation dataset) is textured along $[0001]$ and $[2\bar{1}\bar{1}0]$ with the maximum intensity of ~ 5.8 MRD, it is impossible to make any reliable inverse correlation between the energy of the grain boundaries and their observation frequency in the GBCD plots [60]. While considering

⁶ For the sake of completeness, the characteristic definition of the tilt, twist, symmetric, quasi-symmetric and proper (improper) quasi-symmetric grain boundaries are defined. In the case of a tilt grain boundary, the axis of misorientation is perpendicular to the grain boundary plane normal while in the case of twist grain boundary these two are parallel. The grain boundary plane of a symmetric boundary acts as a mirror between the two crystals associated with the grain boundary. In a quasi-symmetric grain boundary, the grain boundary planes corresponding to both sides of a grain boundary belong to the same crystallographic family. In the case of a proper (improper) quasi-symmetric grain boundary, the relationship between the grain boundary plane normal (m) on both sides of this type of a grain boundary is $m_1 = \pm C_2 m_2$ where C represents proper orthogonal matrices of symmetry operations. Notably, considering inversion symmetry, a symmetric boundary can be considered as a tilt grain boundary. A proper quasi-symmetric boundary is identical to a twist boundary and vice versa. An improper quasi-symmetric grain boundary is the same as a 180° -tilt grain boundary. Also, a symmetric boundary is equivalent to a 180° -twist boundary. It should be noted that these definitions are not exclusive. One grain boundary may fall into multiple classes.

this fact, based on the GBCD plots presented for $[0001]$ GBCD sections, it can be said that planes which are close to the basal pole have the highest peak intensity in comparison to the other planes. The observation of a high-intensity peak at the location of the basal plane is consistent with the $30^\circ/[0001]$ GBCD section for WC/WC boundaries (c/a is close to unity) [56]. However, a similar trend was not observed for α -titanium ($c/a = 1.587$) [28].

3.2. GBCD sections about $[2\bar{1}\bar{1}0]$ axis of misorientation

Based upon molecular dynamics analyses presented in the literature [53] where the 31° , 42° , 61° and 74° misorientation angles were determined to be important, the GBCD sections associated with these angles as well as 92° misorientation angle are studied. For the case of the $31^\circ/[2\bar{1}\bar{1}0]$ GBCD section and its calculated geometrically characteristic boundaries shown in Fig. 8(a and b), a 180° -twist grain boundary at $(0,\bar{3},3,20)$ pole with a population of ~ 40 MRD is observed. In addition, a wide range of tilt grain boundaries with the intensities of ~ 16 – 28 MRD are observed. Based on the grain boundary energy calculations from the molecular dynamics analyses for $[2\bar{1}\bar{1}0]$ tilt grain boundaries of α -titanium [53], within the misorientation interval of 24.2° – 35.2° , a cusp in the tilt boundary energy occurs at 31.39° for $(0,1,\bar{1},3)$. The location of this pole is presented with a brown circle in Fig. 8(b). The magnitude of the same location in the GBCD plot is ~ 24 MRD.

According to molecular dynamics analyses [53], the next energy cusp for $[2\bar{1}\bar{1}0]$ tilt grain boundaries of α -titanium shows up at 42.47° misorientation for $(0,1,\bar{1},2)$ pole. The $42^\circ/[2\bar{1}\bar{1}0]$ GBCD section is plotted in Fig. 8(c). A diffuse peak with ~ 26 MRD intensity around the location of the 180° -twist grain boundary plane is seen. The grain boundary plane associated with the 180° -twist grain boundary is $(0,\bar{5},5,24)$. The intensity of $(0,1,\bar{1},2)$ pole which is illustrated by a brown circle in Fig. 8(d) is ~ 18 MRD.

For the case of $61^\circ/[2\bar{1}\bar{1}0]$ angle/axis of misorientation presented in Fig. 8(e and f), 180° -twist grain boundaries at $(0,12,\bar{12},13)$ and $(0,\bar{8},8,25)$ poles are observed with the intensities of ~ 23 MRD and ~ 18 MRD, respectively. Interestingly, molecular dynamics analyses revealed that for the misorientation interval of 52.5° – 67.1° a cusp at the tilt grain boundary energy plot exists for $(0,1,\bar{1},1)$ pole at 61.35° misorientation [53]. Notably, this pole is very close ($\sim 2.3^\circ$) to the $(0,12,\bar{12},13)$ pole which has the highest intensity in Fig. 8(e). This small difference can be attributed to possible uncertainties (e.g., the angular resolution of ASTAR™/PED technique and binning (cell) size) exist in this study. Therefore, they can be considered equivalent. In addition, twist grain boundaries with the observation

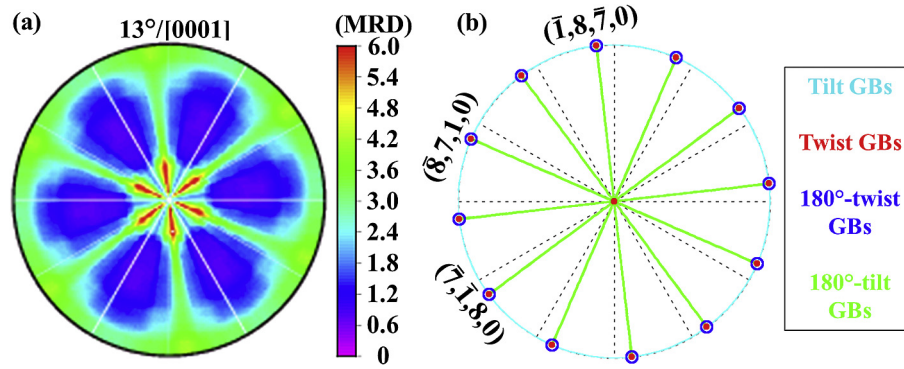


Fig. 7. The distribution of grain boundary planes and their calculated locations of the geometrically characteristic boundaries for $13^\circ/[0001]$ misorientation is shown.

frequency of ~ 10 MRD at $(2, \bar{1}, \bar{1}, 0)$ pole as well as a 180° -tilt grain boundary with the frequency of ~ 8 MRD exist in $61^\circ/[2\bar{1}\bar{1}0]$ GBCD section.

Although the length fraction of grain boundaries with a 74° disorientation is less than random, Fig. 3(c), the $74^\circ/[2\bar{1}\bar{1}0]$ GBCD

section is plotted in Fig. 9(a) to compare the associated grain boundary plane distributions with the calculated grain boundary plane energy for the misorientation interval of 67.1° – 80.5° [53]. Molecular dynamics analyses revealed that the cusp of the grain boundary plane energy for the mentioned misorientation interval

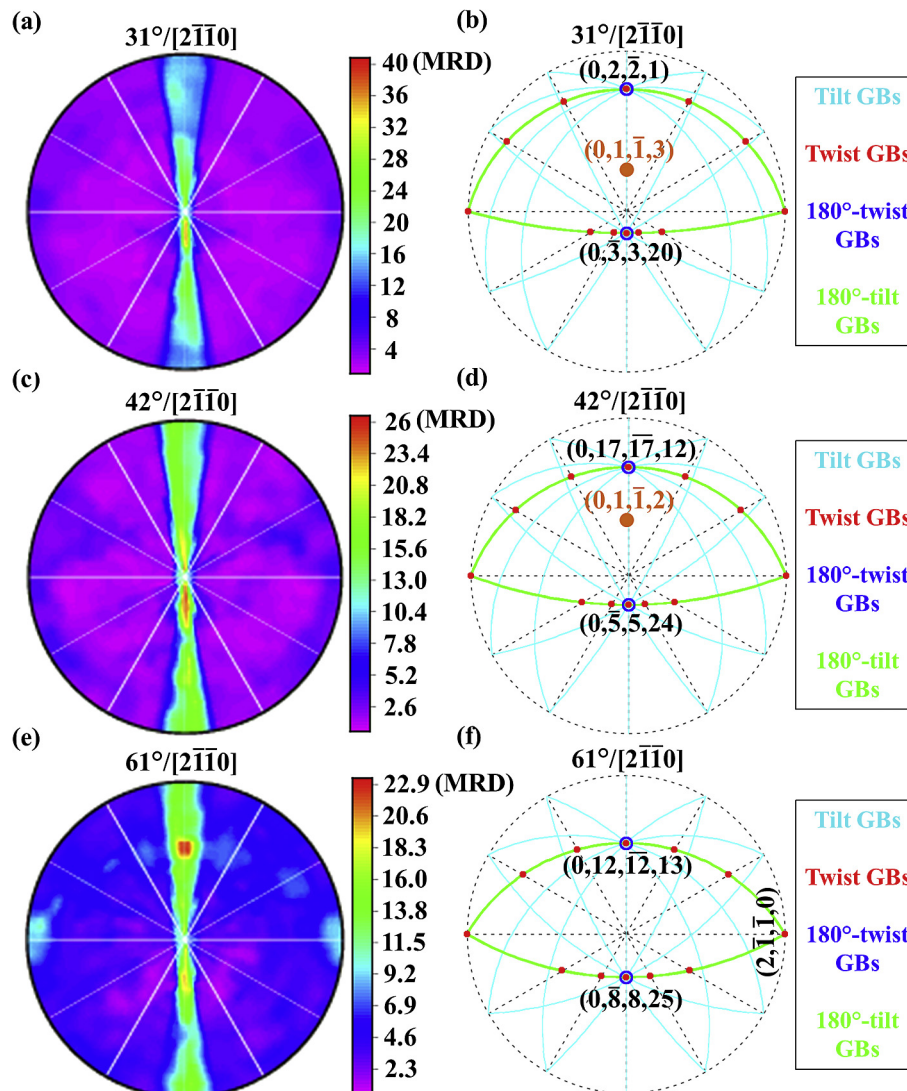


Fig. 8. The distribution of grain boundary planes and their calculated locations of the geometrically characteristic boundaries for (a,b) $31^\circ/[2\bar{1}\bar{1}0]$, (c,d) $42^\circ/[2\bar{1}\bar{1}0]$ and (e,f) $61^\circ/[2\bar{1}\bar{1}0]$ are shown.

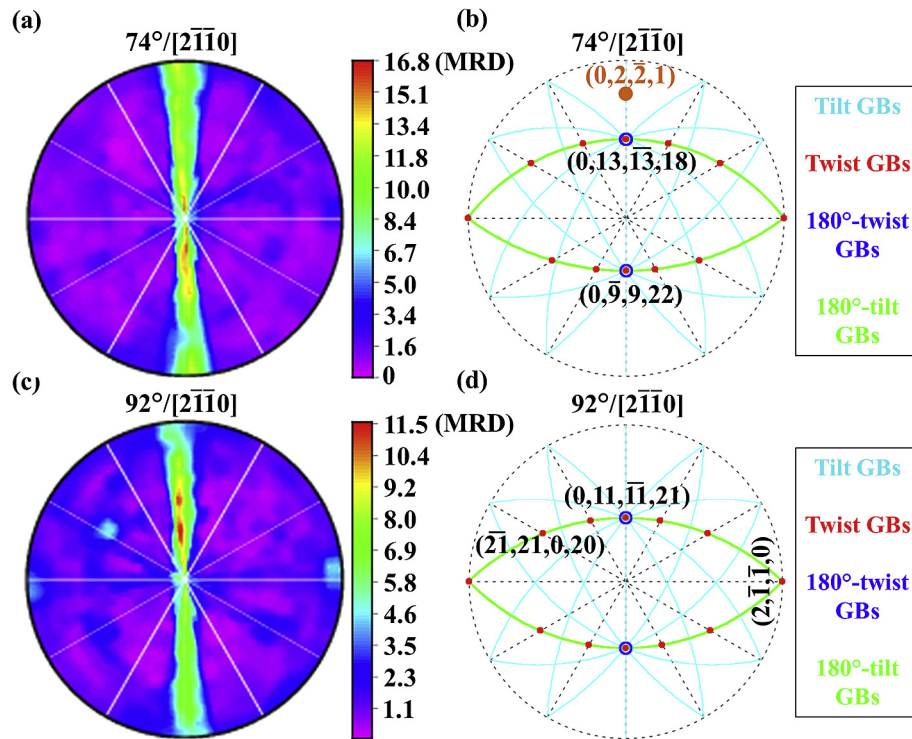


Fig. 9. The distribution of grain boundary planes and their calculated locations of the geometrically characteristic boundaries for (a,b) $74^\circ/[2\bar{1}\bar{1}0]$ and (c,d) $92^\circ/[2\bar{1}\bar{1}0]$ are shown.

belongs to $(0,2,\bar{2},1)$. The location of this pole on the GBCD plot has the magnitude of ~ 11 MRD. The maximum intensity belongs to a diffuse peak along the tilt grain boundaries with the magnitude of ~ 16 MRD. Notably, part of this peak overlaps with a 180° -twist grain boundary with the grain boundary plane of $(0,9,9,22)$, Fig. 9(b).

For the $92^\circ/[2\bar{1}\bar{1}0]$ angle/axis of misorientation, as shown in Fig. 9(c and d) two diffuse peaks close to the $(0,11,\bar{1}\bar{1},21)$ ⁷ pole with a population of ~ 11.5 MRD are detected. These peaks can be considered as grain boundary planes close to a 180° -twist grain boundary plane. Tilt grain boundaries with the intensity of ~ 8 MRD as well as a twist grain boundary at $(2,\bar{1},\bar{1},0)$ pole and close to a twist grain boundary with the grain boundary plane of $(\bar{2}\bar{1},21,0,20)$ ⁸ are seen with the peak intensities of ~ 4.6 MRD. As noted previously, since these planes are so close and the resolution is low, they are indistinguishable from the ideal.

For the GBCD sections presented for $[2\bar{1}\bar{1}0]$ axis of misorientation, the maximum intensity peaks correspond to 180° -twist grain boundaries. Also, GBCD studies of $[2\bar{1}\bar{1}0]$ axis of misorientation for WC [56] and Ti-6Al-4V [29] revealed that high-intensity peaks are associated with 57° , 85° and 90° misorientations. For α -titanium, high-intensity GBCD peaks were observed for 21° , 31° and 75° along $[2\bar{1}\bar{1}0]$ axis of misorientation [28].

3.3. GBCD sections about $[10\bar{1}0]$ axis of misorientation

Based on the molecular dynamics analyses presented in the literature [54] where the 27° , 38° , 58° as well as 72° misorientation angles were determined to be important, the GBCD sections associated with these angles and 90° misorientation angle are studied.

⁷ The $(0,11,\bar{1}\bar{1},21)$ pole is $\sim 1.2^\circ$ far from the $(0,1,\bar{1},2)$ pole. They can be considered equivalent.

⁸ The $(\bar{2}\bar{1},21,0,20)$ is $\sim 1.4^\circ$ far from the $(\bar{1},1,0,1)$ pole. They can be considered equivalent.

Before discussing these GBCD sections, it is important to note that according to the inverse pole figure plot presented in Fig. 3(b), the texture intensity for $\langle 10\bar{1}0 \rangle$ is ~ 1.8 MRD which shows the current combined orientation dataset has fewer observations along $\langle 10\bar{1}0 \rangle$ in comparison to $[0001]$ and $[2\bar{1}\bar{1}0]$. Therefore, one must be cautious when interpreting the GBCD results along $[10\bar{1}0]$ misorientation axis here. For the case of $27^\circ/[10\bar{1}0]$ misorientation, the high-intensity peaks for the GBCD experimental results shown in Fig. 10(a) do not overlap completely with the calculated locations for the geometrically characteristic boundaries presented in Fig. 10(b). This deviation may be due to small experimental uncertainties which can be studied in a quantitative manner. For the grain boundaries observed in Fig. 10(a), the distributions of the angular distances from tilt, twist, 180° -twist and 180° -tilt grain boundaries [61,62] are plotted in Fig. 10(c–f), respectively. The geometrically characteristic boundaries with the lowest angular deviation from the experimental results are the most probable characteristic boundary types.

The locations of the two peaks with the intensity of ~ 9 MRD (surrounded by white ovals in Fig. 10(a)) are drawn in all the four plots in Fig. 10(c–f). These two peaks have an average deviation of $\sim 3.5^\circ$ from pure tilt grain boundaries while the average deviation values increase to far larger values for the pure twist ($\sim 34^\circ$), 180° -twist ($\sim 38^\circ$) and 180° -tilt ($\sim 23^\circ$) grain boundaries. Similar analyses were conducted for the grain boundary planes surrounded by a dashed semi-circle in Fig. 10(a). The grain boundary planes surrounded by the dashed semi-circle have a small distance from pure tilt grain boundaries, Fig. 10(c) and 180° -tilt grain boundaries, Fig. 10(f). Also, some parts of the semi-circle are not largely deviated from pure twist grain boundaries, Fig. 10(d) and a 180° -twist grain boundary, Fig. 10(e). It is probable that the grain boundaries surrounded by the semi-circle are a mixture of different types of mentioned grain boundaries. Molecular dynamics analyses for α -titanium showed that for the misorientation interval of 24° – 34° , a cusp in the tilt grain boundary energy plot exists for $(1,2,1,6)$ pole at

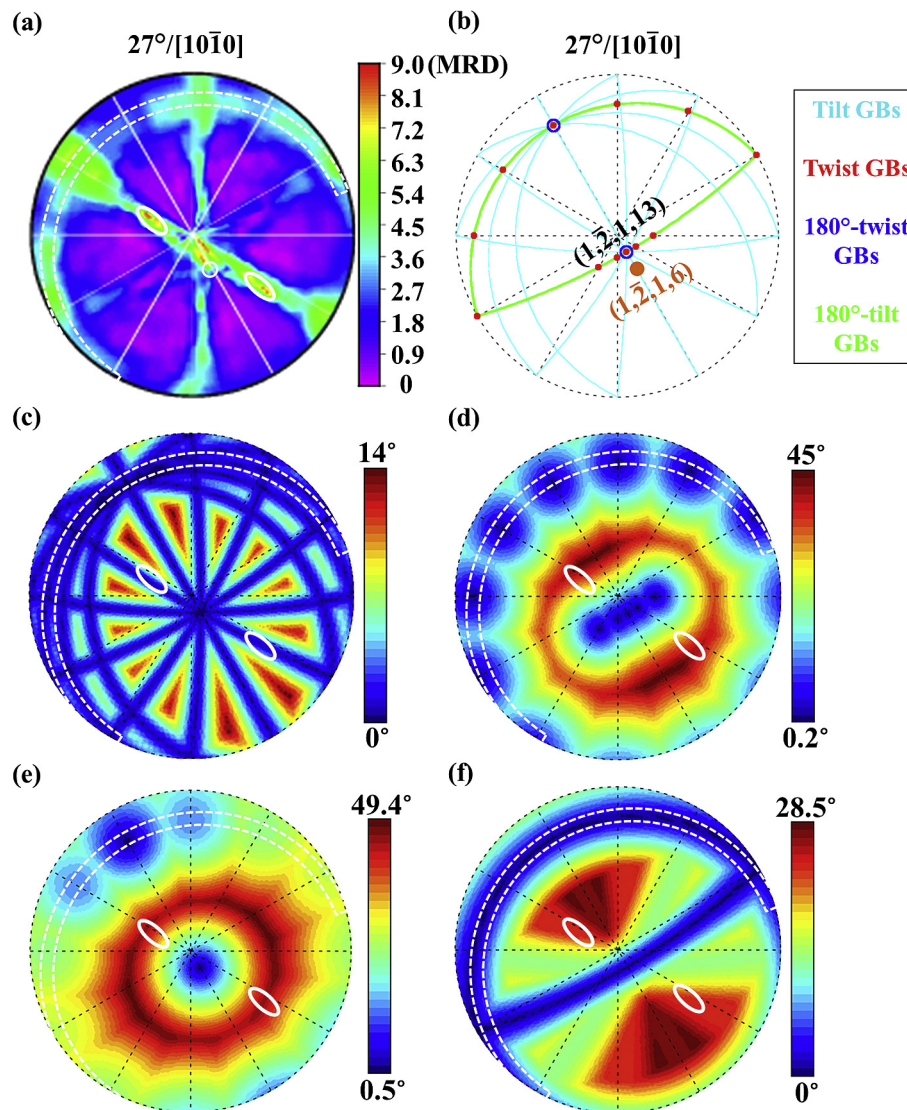


Fig. 10. (a) The distribution of grain boundary planes for $27^\circ/[10\bar{1}0]$ and (b) their calculated locations of the geometrically characteristic boundaries are shown. The associated distributions of the distance of $27^\circ/[10\bar{1}0]$ grain boundary poles to the nearest (c) tilt, (d) twist, (e) 180° -twist and (f) 180° -tilt grain boundaries are presented.

27° misorientation [54]. This pole is presented by a brown point in Fig. 10(b). The same location on the GBCD plot, Fig. 10(a), is surrounded by a white circle. The intensity of this area is ~ 4 MRD. Interestingly, two diffuse peaks with the intensity of ~ 7.2 MRD are observed close to the location of $(1, \bar{2}, 1, 13)$ pole which represents a 180° -twist grain boundary.

For the $38^\circ/[10\bar{1}0]$ GBCD section, as presented in Fig. 11(a and b), a concentrated peak at $(0, 20, \bar{20}, 11)$ ⁹ pole with the magnitude of ~ 8 MRD is observed. This peak represents a twist grain boundary. Also, as shown in Fig. 11(a), some discrete arcs which represent the populations of grain boundary planes corresponding to 180° -tilt grain boundaries are observed with the approximate observation frequency of ~ 6 MRD. Molecular dynamics calculations of α -titanium for the $[10\bar{1}0]$ axis of misorientation within the misorientation interval of 34° – 50° showed that a cusp in the energy of tilt grain boundaries occurs at $(1, \bar{2}, 1, 4)$ [54]. However, for the combined dataset used in this study, the location of $(1, \bar{2}, 1, 4)$ pole in the GBCD plot, Fig. 11 (a), has the intensity of ~ 1 MRD.

In the case of $58^\circ/[10\bar{1}0]$ GBCD section which is shown in Fig. 11(c,d), a peak associated with $(\bar{13}, 26, \bar{13}, 23)$ ¹⁰ pole exists with the magnitude of ~ 5 MRD. This peak represents a 180° -twist grain boundary. Also, an arc which represents 180° -tilt grain boundaries is seen with the intensity of ~ 3.5 MRD. Molecular dynamics analyses for α -titanium within the misorientation interval of 50° – 63° along $[10\bar{1}0]$ misorientation axis showed that $(1, \bar{2}, 1, 2)$ has the local minimum energy [54]. The location of this pole in the GBCD plot has ~ 1 MRD intensity.

The next cusp in the grain boundary energy which is calculated by molecular dynamics analyses is associated with $(1, \bar{2}, 1, 1)$ for the $72.5^\circ/[10\bar{1}0]$ misorientation angle/axis within the misorientation interval of 63° – 79° . The $72^\circ/[10\bar{1}0]$ GBCD section is plotted in Fig. 11(e). The location of $(1, \bar{2}, 1, 1)$ pole in the GBCD plot has the population of less than 1 MRD. Notably, in the GBCD plot, a major peak with the intensity of ~ 4.5 MRD is seen at $(0, 19, \bar{19}, 22)$. This peak represents a twist grain boundary, Fig. 11(f). Two other peaks associated with twist grain boundaries are observed with the

⁹ The $(0, 20, \bar{20}, 11)$ pole is $\sim 2^\circ$ far from the $(0, 2, \bar{2}, 1)$ pole.

¹⁰ The $(\bar{13}, 26, \bar{13}, 23)$ pole is $\sim 3.5^\circ$ far from the $(\bar{1}, 2, \bar{1}, 2)$ pole.

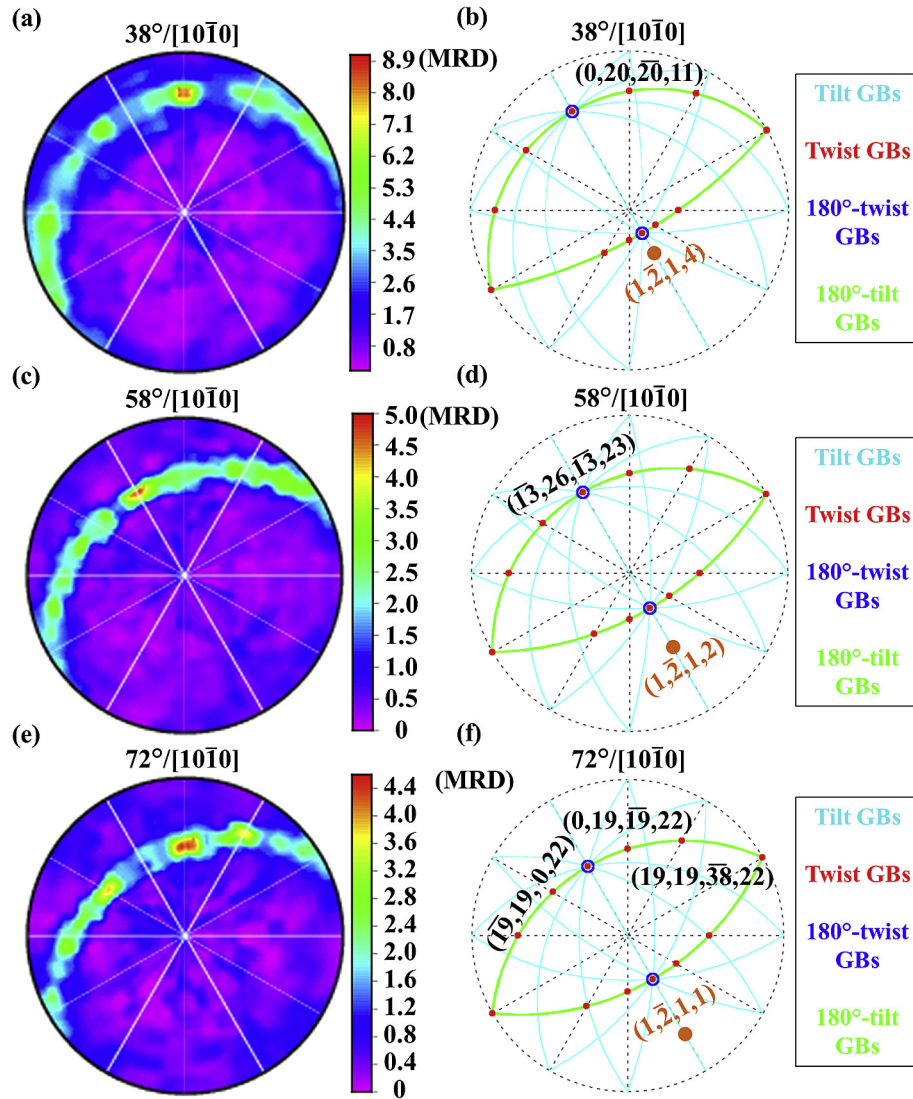


Fig. 11. The distribution of grain boundary planes and their calculated locations of the geometrically characteristic boundaries for (a,b) $38^\circ/[10\bar{1}0]$, (c,d) $58^\circ/[10\bar{1}0]$ and (e,f) $72^\circ/[10\bar{1}0]$ are shown.

approximate intensity of ~ 3.6 MRD at $(\bar{1}9,19,0,22)$ and $(19,19,\bar{3}8,22)$ poles. Also, an arc which represents 180° -tilt grain boundaries is seen with the average intensity of ~ 2 MRD.

Finally, for the $90^\circ/[10\bar{1}0]$ angle and axis of misorientation which is not shown here, a peak with the intensity of ~ 6.6 MRD is detected at $(1,0,\bar{1},0)$ pole which clearly represents a pure twist grain boundary. In general, peaks with the maximum intensity show up at locations belong to either twist or 180° -twist grain boundaries for the $[10\bar{1}0]$ GBCD sections.

In the literature, for the case of tungsten carbide, a high-intensity peak was observed at $(1,0,\bar{1},0)$ pole for the $90^\circ/[10\bar{1}0]$ GBCD section [56]. For α -titanium, high-intensity GBCD peaks for $[10\bar{1}0]$ axis of misorientation were observed for 22° and 90° misorientations [28]. The inconsistency between the molecular dynamics results (i.e., energy of the grain boundaries) [53,54] and the GBCD results (i.e., the population of grain boundaries) for α -titanium [28] might be attributed to the fact that the energy of the grain boundaries were calculated at 0 K while the microstructure studied by the GBCD method formed at high temperature. Also, for the case of $[10\bar{1}0]$ grain boundaries, the calculated energy values for the cusps are not considerably lower than the energies of boundaries which are 5° away. Therefore, inconsistency between the GBCD results and the

molecular dynamics results are expected. Interestingly, in the case of $61^\circ/[2\bar{1}\bar{1}0]$ grain boundaries, due to a remarkable difference between the cusp energy and the energy of grain boundaries which are 5° away, very good consistency between molecular dynamics results of α -titanium and the GBCD plot of zirconium, Fig. 8(e) is observed. As noted, the study of grain boundaries, their populations, and the attempted correlations with energy is a complex problem [63]. For example, these small changes in both the depth of the energy cusp and the relative energy of boundaries X° away are directly related to the full energy landscape (here, in a five parameter space). Within the five-parameter grain boundary space, the relative position (i.e., the grain boundary configuration) of these energy cusps, as well as their depths, will ultimately determine the populations of grain boundaries under various regimes (e.g., non-equilibrium vs equilibrium).

3.4. $90^\circ/[4\bar{1}\bar{3}1]$ GBCD section

Based on the distribution of grain boundaries in the angle/axis space, shown in Fig. 5, it was noticed that the distribution of $90^\circ/[4\bar{1}\bar{3}1]$ is more than uniform (~ 4 MRD). The GBCD section associated with $90^\circ/[4\bar{1}\bar{3}1]$ is illustrated in Fig. 12(a). Since no exact

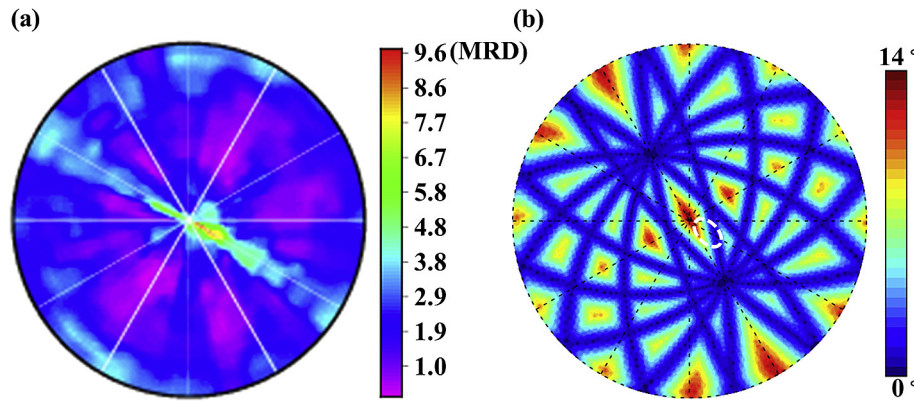


Fig. 12. (a) The distribution of grain boundary planes for $90^\circ/[4\bar{1}\bar{3}1]$ and (b) the associated distributions of the distance of $90^\circ/[4\bar{1}\bar{3}1]$ grain boundary pole (white oval) to the nearest tilt grain boundaries are presented.

match was found between the location of the maximum-intensity peak (~ 9.6 MRD) in the GBCD plot with the calculated locations of the geometrically characteristic boundaries associated with $90^\circ/[4\bar{1}\bar{3}1]$, the distance distributions of the $90^\circ/[4\bar{1}\bar{3}1]$ grain boundary poles from the nearest tilt, twist, 180° -twist and 180° -tilt grain boundaries were determined. The minimum deviation from these grain boundaries was found to be consistent with a pure tilt grain boundary, Fig. 12 (b).

3.5. Using this data: beyond grain boundary engineering

As noted previously, the data of these types of GBCD studies is incredibly rich, and the analysis can provide new information for both current and emerging materials science problems. For example, the GBCD plots presented in this study provide new horizons to not only guide interpretations of new research areas, but also reflect upon previous studies on zirconium. For instance, while hydride formation in zirconium is a function of crystallographic texture which follows hydride habit planes [64], the possibility of hydride formation at the grain boundaries of zirconium was assessed only based on the associated angle and axis of misorientation for each grain boundary [65]. It is claimed that $25^\circ/[0001]$, $85^\circ/\langle 2\bar{1}\bar{1}0 \rangle$ and $85^\circ/\langle 10\bar{1}0 \rangle$ angle/axis of misorientations resist to hydriding while $25^\circ/\langle 10\bar{1}0 \rangle$ favors the formation of hydrides. The GBCD plots of the current study show that for each angle/axis misorientation pair a wide range of grain boundary types with considerably different populations of grain boundary planes may exist. These grain boundary planes and their populations should be considered when different properties of zirconium (e.g., the possibility of hydride formation) are investigated. Similarly, using fine-grained materials may guide new fundamental studies of grain boundary populations that are important for many other properties, including other phase transformations and variant selection; mechanical properties mediated by deformation processes along grain boundaries or by fracture mechanics; and electrical transport properties that can be a function of grain boundary configurations.

4. Conclusions

The grain boundary character distribution of nanocrystalline α -zirconium was studied using a statistical method. The orientation datasets of the thin films were acquired by ASTAR™/precession electron diffraction technique thanks to its remarkably high spatial resolution. In general, the results demonstrate that highly refined

(nanoscaled) grains can be used to obtain large datasets of grain boundary types that can be probed to understand the grain boundary character distributions. When material is produced using physical vapor deposition, the material consists of columnar grains that can be confirmed using grain boundary trace analysis, and the grains can be relatively textured (here, the texture intensity along $[0001]$, $\langle 2\bar{1}\bar{1}0 \rangle$ and $\langle 10\bar{1}0 \rangle$ were 5.8 MRD, 5.8 MRD and 1.8 MRD, respectively).

For this database, the following seven observations can be drawn.

- The distribution of disorientation angles was larger than the random condition except for the disorientation intervals of 40° – 57° and 60° – 90° .
- The distribution of grain boundaries in axis-angle space showed peaks larger than the random distribution along the $[0001]$, $[2\bar{1}\bar{1}0]$, $[10\bar{1}0]$ and $[4\bar{1}\bar{3}1]$ axes.
- The highest population of grain boundary planes in the crystal reference frame was observed at the basal plane with the magnitude of ~ 2 MRD. For the $(1,0,\bar{1},0)$ and $(2,\bar{1},\bar{1},0)$ planes, the populations were ~ 1.8 and ~ 1.4 MRD, respectively.
- For the GBCD section of the $[0001]$ misorientation, the highest population of grain boundaries was observed for the misorientation angle of 13° .
- For the case of $[2\bar{1}\bar{1}0]$ misorientation axis, the maximum intensity in the GBCD plot was observed at (or close to) the 180° -twist grain boundaries for the misorientations of 31° , 42° , 61° , 74° and 92° .
- GBCD plots for $[10\bar{1}0]$ axis and 27° , 38° , 58° , 72° and 90° misorientation angles showed that the maximum peak in each plot is associated with either twist or 180° -twist grain boundaries.
- For the GBCD section of $90^\circ/[4\bar{1}\bar{3}1]$, grain boundaries slightly deviated from a pure tilt grain boundary have the highest intensity.

Acknowledgements

The authors gratefully acknowledge the Iowa State University, Ames Laboratory and the Center for Advanced Non-Ferrous Structural Alloys, which is a joint industry–university center between the Colorado School of Mines and the Iowa State University (NSF award no. 1624748).

References

- [1] P. Davies, V. Randle, Grain boundary engineering and the role of the interfacial plane, *Mater. Sci. Technol.* 17 (6) (2001) 615–626.
- [2] T. Watanabe, Grain boundary engineering: historical perspective and future prospects, *J. Mater. Sci.* 46 (12) (2011) 4095–4115.
- [3] V. Randle, Role of grain boundary plane in grain boundary engineering, *Mater. Sci. Technol.* 26 (7) (2010) 774–780.
- [4] V. Randle, Grain boundary engineering: an overview after 25 years, *Mater. Sci. Technol.* 26 (3) (2010) 253–261.
- [5] P.R. Cantwell, S. Ma, S.A. Bojarski, G.S. Rohrer, M.P. Harmer, Expanding time–temperature–transformation (TTT) diagrams to interfaces: a new approach for grain boundary engineering, *Acta Mater.* 106 (2016) 78–86.
- [6] P. Lin, G. Palumbo, U. Erb, K. Aust, Influence of grain boundary character distribution on sensitization and intergranular corrosion of alloy 600, *Scr. Metall. Mater.* 33 (9) (1995) 1387–1392.
- [7] C.-S. Kim, Y. Hu, G.S. Rohrer, V. Randle, Five-parameter grain boundary distribution in grain boundary engineered brass, *Scr. Mater.* 52 (7) (2005) 633–637.
- [8] V. Randle, The Role of the Coincidence Site Lattice in Grain Boundary Engineering, Maney Pub, 1996.
- [9] G. Herrmann, H. Gleiter, G. Bärö, Investigation of low energy grain boundaries in metals by a sintering technique, *Acta Metall.* 24 (4) (1976) 353–359.
- [10] P. Goodhew, R. Allen, Comments on: “Low energy grain boundaries in metals” by Herrmann, Gleiter and Bärö, *Acta Met. Scr. Metall.* 11 (1) (1977) 37–39.
- [11] C.-S. Kim, A.D. Rollett, G.S. Rohrer, Grain boundary planes: new dimensions in the grain boundary character distribution, *Scr. Mater.* 54 (6) (2006) 1005–1009.
- [12] G.S. Rohrer, V. Randle, C.-S. Kim, Y. Hu, Changes in the five-parameter grain boundary character distribution in α -brass brought about by iterative thermomechanical processing, *Acta Mater.* 54 (17) (2006) 4489–4502.
- [13] V. Randle, ‘Special’ boundaries and grain boundary plane engineering, *Scr. Mater.* 54 (6) (2006) 1011–1015.
- [14] P.R. Cantwell, M. Tang, S.J. Dillon, J. Luo, G.S. Rohrer, M.P. Harmer, Grain boundary complexes, *Acta Mater.* 62 (2014) 1–48.
- [15] A.P. Sutton, R.W. Balluffi, *Interfaces in Crystalline Materials*, 1995.
- [16] C. Goux, Structure des joints de grains: considérations cristallographiques et méthodes de calcul des structures, *Can. Metall. Q.* 13 (1) (1974) 9–31.
- [17] G.S. Rohrer, D.M. Saylor, B. El-Dasher, B.L. Adams, A.D. Rollett, P. Wynblatt, The distribution of internal interfaces in polycrystals, *Z. Met.* 95 (4) (2004) 197–214.
- [18] D.M. Saylor, A. Morawiec, G.S. Rohrer, Distribution of grain boundaries in magnesia as a function of five macroscopic parameters, *Acta Mater.* 51 (13) (2003) 3663–3674.
- [19] K. Glowinski, A. Morawiec, Analysis of experimental grain boundary distributions based on boundary-space metrics, *Metall. Mater. Trans. A* 45 (8) (2014) 3189–3194.
- [20] D.M. Saylor, B.S. El Dasher, A.D. Rollett, G.S. Rohrer, Distribution of grain boundaries in aluminum as a function of five macroscopic parameters, *Acta Mater.* 52 (12) (2004) 3649–3655.
- [21] H.M. Miller, D. Saylor, B.S. El Dasher, A.D. Rollett, G.S. Rohrer, Crystallographic distribution of internal interfaces in spinel polycrystals, *Mater. Sci. Forum, Trans. Tech. Publ.* (2004) 783–788.
- [22] D.M. Saylor, B. Dasher, T. Sano, G.S. Rohrer, Distribution of grain boundaries in SrTiO₃ as a function of five macroscopic parameters, *J. Am. Ceram. Soc.* 87 (4) (2004) 670–676.
- [23] D.M. Saylor, B. Dasher, Y. Pang, H.M. Miller, P. Wynblatt, A.D. Rollett, G.S. Rohrer, Habits of grains in dense polycrystalline solids, *J. Am. Ceram. Soc.* 87 (4) (2004) 724–726.
- [24] T.A. Bennett, C.S. Kim, G.S. Rohrer, A.D. Rollett, Five-parameter grain boundary character distribution in Fe-1% Si, *Mater. Sci. Forum Trans. Tech. Publ.* (2004) 727–732.
- [25] G.S. Rohrer, Influence of interface anisotropy on grain growth and coarsening, *Annu. Rev. Mater. Res.* 35 (2005) 99–126.
- [26] D.M. Saylor, A. Morawiec, G.S. Rohrer, The relative free energies of grain boundaries in magnesia as a function of five macroscopic parameters, *Acta Mater.* 51 (13) (2003) 3675–3686.
- [27] D.M. Saylor, A. Morawiec, G.S. Rohrer, Distribution and energies of grain boundaries in magnesia as a function of five degrees of freedom, *J. Am. Ceram. Soc.* 85 (12) (2002) 3081–3083.
- [28] M.N. Kelly, K. Glowinski, N.T. Nuhfer, G.S. Rohrer, The five parameter grain boundary character distribution of α -Ti determined from three-dimensional orientation data, *Acta Mater.* 111 (2016) 22–30.
- [29] V. Randle, G. Rohrer, Y. Hu, Five-parameter grain boundary analysis of a titanium alloy before and after low-temperature annealing, *Scr. Mater.* 58 (3) (2008) 183–186.
- [30] H. Beladi, Q. Chao, G.S. Rohrer, Variant selection and intervariant crystallographic planes distribution in martensite in a Ti–6Al–4V alloy, *Acta Mater.* 80 (0) (2014) 478–489.
- [31] A. Darbal, K. Ganesh, X. Liu, S.-B. Lee, J. Ledonne, T. Sun, B. Yao, A. Warren, G. Rohrer, A. Rollett, P. Ferreira, K. Coffey, K. Barmak, Grain boundary character distribution of nanocrystalline Cu thin films using stereological analysis of transmission electron microscope orientation maps, *Microsc. Microanal.* 19 (01) (2013) 111–119.
- [32] V. Randle, G. Rohrer, H. Miller, M. Coleman, G. Owen, Five-parameter grain boundary distribution of commercially grain boundary engineered nickel and copper, *Acta Mater.* 56 (10) (2008) 2363–2373.
- [33] X. Liu, D. Choi, H. Beladi, N.T. Nuhfer, G.S. Rohrer, K. Barmak, The five-parameter grain boundary character distribution of nanocrystalline tungsten, *Scr. Mater.* 69 (5) (September 2013) 413–416. ISSN 1359-6462.
- [34] S. Zaefferer, On the formation mechanisms, spatial resolution and intensity of backscatter Kikuchi patterns, *Ultramicroscopy* 107 (2) (2007) 254–266.
- [35] D.R. Steinmetz, T. Jäpel, B. Wietbrock, P. Eisenlohr, I. Gutierrez-Urrutia, A. Saeed-Akbari, T. Hickel, F. Roters, D. Raabe, Revealing the strain-hardening behavior of twinning-induced plasticity steels: theory, simulations, experiments, *Acta Mater.* 61 (2) (2013) 494–510.
- [36] S. Dancette, L. Delannay, K. Renard, M. Melchior, P. Jacques, Crystal plasticity modeling of texture development and hardening in TWIP steels, *Acta Mater.* 60 (5) (2012) 2135–2145.
- [37] N. Brodusch, H. Demers, R. Gauvin, Nanometres-resolution Kikuchi patterns from materials science specimens with transmission electron forward scatter diffraction in the scanning electron microscope, *J. Microsc.* 250 (1) (2013) 1–14.
- [38] P.W. Trimby, Orientation mapping of nanostructured materials using transmission Kikuchi diffraction in the scanning electron microscope, *Ultramicroscopy* 120 (0) (2012) 16–24.
- [39] P.W. Trimby, Y. Cao, Z. Chen, S. Han, K.J. Hemker, J. Lian, X. Liao, P. Rottmann, S. Samudrala, J. Sun, J.T. Wang, J. Wheeler, J.M. Cairney, Characterizing deformed ultrafine-grained and nanocrystalline materials using transmission Kikuchi diffraction in a scanning electron microscope, *Acta Mater.* 62 (0) (2014) 69–80.
- [40] D. Viladot, M. Véron, M. Gemmi, F. Peiró, J. Portillo, S. Estradé, J. Mendoza, N. Llorca-Isern, S. Nicolopoulos, Orientation and phase mapping in the transmission electron microscope using precession-assisted diffraction spot recognition: state-of-the-art results, *J. Microsc.* 252 (1) (2013) 23–34.
- [41] E.F. Rauch, M. Véron, Automated crystal orientation and phase mapping in TEM, *Mater. Charact.* 98 (0) (2014) 1–9.
- [42] I. Ghamarian, Y. Liu, P. Samimi, P.C. Collins, Development and application of a novel precession electron diffraction technique to quantify and map deformation structures in highly deformed materials—as applied to ultrafine-grained titanium, *Acta Mater.* 79 (0) (2014) 203–215.
- [43] J.G. Brons, G.B. Thompson, A comparison of grain boundary evolution during grain growth in fcc metals, *Acta Mater.* 61 (11) (2013) 3936–3944.
- [44] T. White, A. Eggeman, P. Midgley, Is precession electron diffraction kinematical? Part I: “Phase-scrambling” multislice simulations, *Ultramicroscopy* 110 (7) (2010) 763–770.
- [45] A. Eggeman, T. White, P. Midgley, Is precession electron diffraction kinematical? Part II: A practical method to determine the optimum precession angle, *Ultramicroscopy* 110 (7) (2010) 771–777.
- [46] E.F. Rauch, J. Portillo, S. Nicolopoulos, D. Bultreys, S. Rouvimov, P. Moeck, Automated nanocrystal orientation and phase mapping in the transmission electron microscope on the basis of precession electron diffraction, *Z. Krist.* 225 (2–3) (2010) 103–109.
- [47] H. Beladi, G.S. Rohrer, The relative grain boundary area and energy distributions in a ferritic steel determined from three-dimensional electron backscatter diffraction maps, *Acta Mater.* 61 (4) (2013) 1404–1412.
- [48] X. Liu, N. Nuhfer, A. Rollett, S. Sinha, S.-B. Lee, J. Carpenter, J. LeDonne, A. Darbal, K. Barmak, Interfacial orientation and misorientation relationships in nanolamellar Cu/Nb composites using transmission-electron-microscope-based orientation and phase mapping, *Acta Mater.* 64 (2013) 333–344.
- [49] D.B. Williams, C.B. Carter, *Transmission Electron Microscopy: a Textbook for Materials Science*, second ed., Springer, New York, 2009.
- [50] E. Rauch, L. Dupuy, Rapid spot diffraction patterns identification through template matching, *Arch. Metall. Mater.* 50 (2005) 87–99.
- [51] M. Seita, M. Volpi, S. Patala, I. McCue, C.A. Schuh, M.V. Diamanti, J. Erlebacher, M.J. Demkowicz, A high-throughput technique for determining grain boundary character non-destructively in microstructures with through-thickness grains, *Npj Comput. Mater.* 2 (2016) 16016.
- [52] S. Wright, R. Larsen, Extracting twins from orientation imaging microscopy scan data, *J. Microsc.* 205 (3) (2002) 245–252.
- [53] J. Wang, I.J. Beyerlein, Atomic structures of symmetric tilt grain boundaries in hexagonal close packed (hcp) crystals, *Model. Simul. Mater. Sci. Eng.* 20 (2) (2012) 024002.
- [54] J. Wang, I.J. Beyerlein, Atomic structures of Σ [0 $\bar{1}$ 10] Σ symmetric tilt grain boundaries in hexagonal close-packed (hcp) crystals, *Metall. Mater. Trans. A* 43 (10) (2012) 3556–3569.
- [55] Y. Hu, V. Randle, An electron backscatter diffraction analysis of misorientation distributions in titanium alloys, *Scr. Mater.* 56 (12) (2007) 1051–1054.
- [56] C.S. Kim, T.R. Massa, G.S. Rohrer, Interface character distributions in WC–Co composites, *J. Am. Ceram. Soc.* 91 (3) (2008) 996–1001.
- [57] J. Li, S.J. Dillon, G.S. Rohrer, Relative grain boundary area and energy distributions in nickel, *Acta Mater.* 57 (14) (2009) 4304–4311.
- [58] K. Glowinski, *Methods for Quantitative Characterization of Three-dimensional*

- Grain Boundary Networks in Polycrystalline Materials, Institute of Metallurgy and Materials Science, Polish Academy of Sciences, 2015, 836076817X.
- [59] A. Morawiec, On 'interface-plane scheme' and symmetric grain boundaries, *Z. für Kristallogr. Cryst. Mater.* 227 (4) (2012) 199–206.
- [60] G.S. Rohrer, Grain boundary energy anisotropy: a review, *J. Mater. Sci.* 46 (18) (2011) 5881–5895.
- [61] A. Morawiec, K. Glowinski, On "macroscopic" characterization of mixed grain boundaries, *Acta Mater.* 61 (15) (2013) 5756–5767.
- [62] K. Glowinski, On identification of symmetric and improperly quasi-symmetric grain boundaries, *J. Appl. Crystallogr.* 47 (2) (2014) 726–731.
- [63] G.S. Rohrer, E.A. Holm, A.D. Rollett, S.M. Foiles, J. Li, D.L. Olmsted, Comparing calculated and measured grain boundary energies in nickel, *Acta Mater.* 58 (15) (2010) 5063–5069.
- [64] V. Arunachalam, B. Lehtinen, G. Östberg, The orientation of zirconium hydride on grain boundaries in zircaloy-2, *J. Nucl. Mater.* 21 (3) (1967) 241–248.
- [65] K.M. Krishna, A. Sain, I. Samajdar, G. Dey, D. Srivastava, S. Neogy, R. Tewari, S. Banerjee, Resistance to hydride formation in zirconium: an emerging possibility, *Acta Mater.* 54 (18) (2006) 4665–4675.